




Article

Improving Sea Ice Characterization in Dry Ice Winter Conditions Using Polarimetric Parameters from C- and L-Band SAR Data

Mohammed Dabboor ^{1,*} , Benoit Montpetit ^{2,3} , Stephen Howell ⁴  and Christian Haas ⁵

¹ Meteorological Research Division, Environment and Climate Change Canada, Dorval, QC H9P 1J3, Canada

² Canadian Ice Service, Environment and Climate Change Canada, Ottawa, ON K1A 0H3, Canada; Benoit.Montpetit2@canada.ca

³ National Wildlife Research Center, Environment and Climate Change Canada, Ottawa, ON K1A 0H3, Canada

⁴ Climate Research Division, Environment and Climate Change Canada, Toronto, ON M3H 5T4, Canada; Stephen.Howell@canada.ca

⁵ Department of Earth and Space Science and Engineering, York University, Toronto, ON M3J 1P3, Canada; Hassc@york.ca

* Correspondence: Mohammed.Dabboor@canada.ca; Tel.: +1-514-421-4756

Received: 31 October 2017; Accepted: 4 December 2017; Published: 7 December 2017

Abstract: Sea ice monitoring and classification is one of the main applications of Synthetic Aperture Radar (SAR) remote sensing. C-band SAR imagery is regarded as an optimal choice for sea ice applications; however, other SAR frequencies has not been extensively assessed. In this study, we evaluate the potential of fully polarimetric L-band SAR imagery for monitoring and classifying sea ice during dry winter conditions compared to fully polarimetric C-band SAR. Twelve polarimetric SAR parameters are derived using sets of C- and L-band SAR imagery and the capabilities of the derived parameters for the discrimination between First Year Ice (FYI) and Old Ice (OI), which is considered to be a mixture of Second Year Ice (SYI) and Multiyear Ice (MYI), are investigated. Feature vectors of effective C- and L-band polarimetric parameters are extracted and used for sea ice classification. Results indicate that C-band SAR provides high classification accuracy (98.99%) of FYI and OI in comparison to the obtained accuracy using L-band SAR (82.17% and 81.85%), as expected. However, L-band SAR was found to classify only the MYI floes as OI, while merging both FYI and SYI into one separate class. This comes in contrary to C-band SAR, which classifies as OI both MYI and SYI. This indicates a new potential for discriminating SYI from MYI by combining C- and L-band SAR in dry ice winter conditions.

Keywords: L-band SAR; sea ice; polarimetric parameters; classification

1. Introduction

One of the earliest applications of Synthetic Aperture Radar (SAR) imagery was the classification of sea ice [1]. Most of the early sea ice classification studies were conducted using single polarized C-band SAR data from ERS-1 [2–5], ERS-2 [6–8] and RADARSAT-1 [1,8–11] SAR systems. The first multifrequency fully polarimetric SAR measurements over sea ice were airborne SAR data acquired in 1988 and introduced in [12]. Herein, the polarimetric SAR signatures of different sea ice types were studied for the first time in C-, L-, and P-band. In [12], it was first reported that using various combinations of radar wavelength and polarization was advantageous for enhancing the capability to distinguish between different sea ice types.

C-band SAR imagery has been widely used for sea ice extent and area classification as well as concentration estimation [13,14]. This is because C-band SAR frequency provides a good compromise

between X- and L-band SAR frequencies, which makes it better especially during winter for sea ice classification and ice/open water discrimination [15]. However, other SAR frequencies might also be useful for sea ice monitoring [14,16–18]. L-band SAR imagery in particular has been found superior for identifying deformation features, such as ice ridges, rubble fields, and brash ice [16,17,19]. In contrary to C-band, L-band SAR imagery proved useful in the separation between wind-roughened open water and sea ice [17,20,21]. Furthermore, it was found to provide significantly improved discrimination capability between First Year Ice (FYI) and Multiyear Ice (MYI) in linear horizontal polarization (HH) imagery during the melt season [22]. The usefulness of L-band SAR imagery as a complementary source of information to identify leads in ice and newly formed sea ice was presented in [14]. Compared to C-band, L-band SAR showed larger intensity contrasts between new and level ice [19]. An attempt to use L-band SAR imagery for sea ice thickness estimation was presented in [23]. Moreover, the effectiveness of L-band polarimetric SAR data for sea ice monitoring by using an airborne Polarimetric and Interferometric SAR (PI-SAR) system was discussed in [24]. The dependencies of a set of polarimetric parameters on radar incidence angles for thin ice, smooth FYI, and rough FYI were studied. The studied parameters suggested that the polarimetric coherence and the phase difference between the circular polarization backscattering coefficients RR (right-right) and LL (left-left) were found useful for the discrimination between the tested ice types [24]. Overall, the improved performance of L-band SAR is largely attributed to its high penetration in sea ice, ~0.5 m [25,26], due to the long wavelength of the radar signal which makes it less sensitive to surface properties [17,27]. Although the aforementioned studies highlight the potential of L-band SAR imagery, the sensitivity of L-band polarimetric SAR parameters to ice type differences has yet to be extensively analyzed.

This paper describes the results of the analysis of polarimetric sea ice SAR data acquired by the Phased-Array L-band SAR-2 (PALSAR-2) aboard the Advanced Land Observing Satellite-2 (ALOS-2) over the Victoria Strait in the Canadian Arctic Archipelago (CAA). The polarimetric signatures of thick FYI and Old Ice (OI) are qualitatively and quantitatively analyzed in sets of polarimetric parameters extracted from ALOS-2 full polarimetric L-band SAR data. Sea ice signatures in the L-band polarimetric parameters are compared with the sea ice signatures in C-band polarimetric parameters extracted from overlapped C-band full polarimetric RADARSAT-2 SAR data. Histograms of FYI and OI in each polarimetric parameter for both C- and L-band SAR are derived and analyzed. Furthermore, the mutual information between the two ice types in each polarimetric parameter and the correlation between parameters are estimated. Finally, the Random Forest (RF) classification algorithm is applied on the most effective of the polarimetric parameters to classify both C- and L-band imagery and the results are compared with regional ice charts of the Canadian Ice Service (CIS) and in situ observation data.

2. SAR Imagery and Ice Conditions

The Victoria Strait region in the CAA (Figure 1) was selected as a primary study area. The CAA is an ideal area for testing classification because there is generally a wide range of ice types in this area and ice dynamics is negligible during winter. Images from RADARSAT-2 and ALOS-2 satellites were collected in April 2015 in dry ice winter conditions. As shown in Figure 1, three full polarimetric SAR images from RADARSAT-2 (one) and ALOS-2 (two) were available over the study area. We also used imagery acquired over Hudson Bay to confirm ice type classification results, as Hudson Bay is known to only contain seasonal FYI. Over Hudson Bay, one ALOS-2 full polarimetric SAR image was acquired (Figure 1). The images have Noise-Equivalent Sigma Zero (NESZ) better than -35 dB in HH and VV co-polarized channels and -45 dB in HV and VH cross-polarized channels for RADARSAT-2 [28] and -36 dB in HH and VV co-polarized channels and -46 dB in HV and VH cross-polarized channels for ALOS-2 [29]. During April 2015, the air temperature was always below zero (Figure 2), with a mean value of -21.3 °C according to archived weather data from the Gjoa Haven weather station in Nunavut, which is ~175 km southeast of the study area on King William Island. Summary of the available SAR data is shown in Table 1.

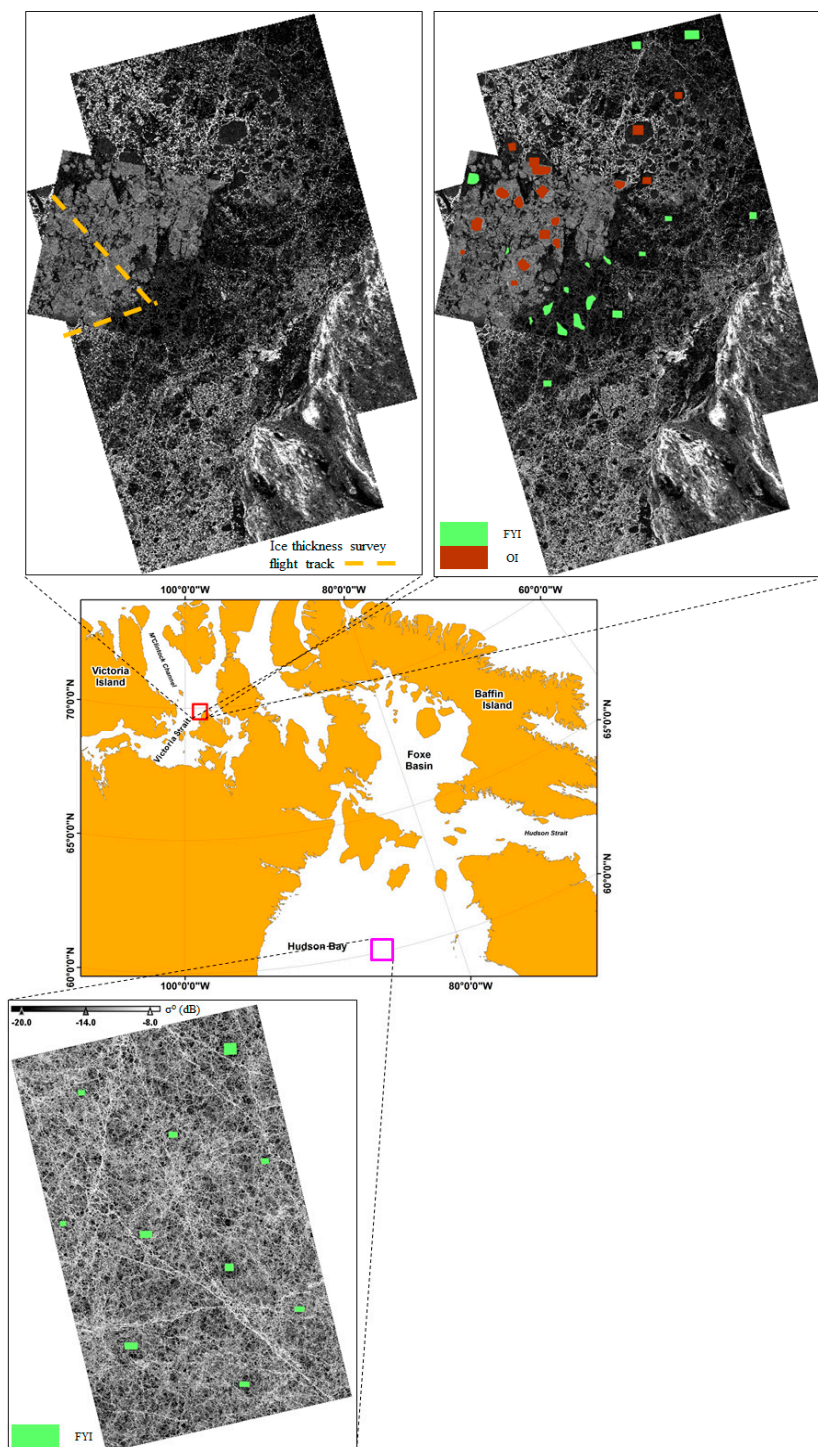


Figure 1. Location of the study area (red square) in the Canadian Arctic Archipelago (CAA). Also shown are the total backscattering power (SPAN) of the RADARSAT-2 image and the two Advanced Land Observing Satellite-2 (ALOS-2) images with the ice thickness survey flight track and the selected First Year Ice (FYI) (green) and Old Ice (OI) (brown) samples. SPAN of ALOS-2 image over Hudson Bay is shown with the location (magenta square) and the selected FYI samples.

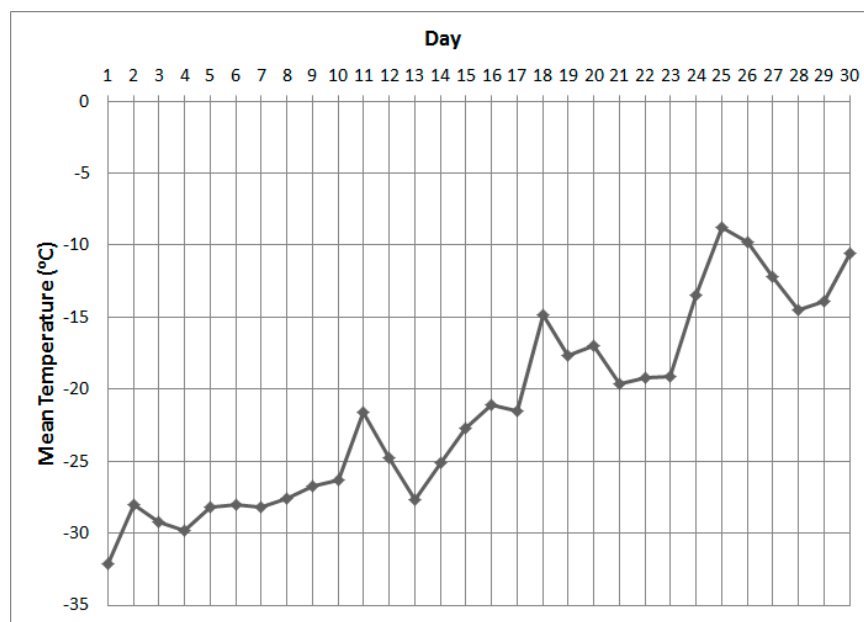


Figure 2. Daily mean temperature for April 2015 recorded at the Gjoa Haven weather station.

Table 1. Summary of Synthetic Aperture Radar (SAR) image acquisitions.

Image	Acquisition Date and Time	Location	Orbit Direction	Incidence Angle	Pixel Spacing (rng × az)	Swath
RADARSAT-2 Fine Quad-Pol	23 April 2015 13:08:56 UTC	Victoria Strait	Descending	40.9°	4.7 m × 5.1 m	27.3 km
ALOS-2 PALSAR-2	5 April 2015 05:51:34 UTC	Victoria Strait	Ascending	36.6°	2.9 m × 2.8 m	41.5 km
ALOS-2 PALSAR-2	28 April 2015 05:44:36 UTC	Victoria Strait	Ascending	31.1°	2.9 m × 3.1 m	41.5 km
ALOS-2 PALSAR-2	22 April 2015 05:14:04 UTC	Hudson Bay	Ascending	33.9°	2.9 m × 3.2 m	41.5 km

Regional sea ice charts produced by Environment and Climate Change Canada at the CIS were acquired for this study from the CIS website (<https://www.ec.gc.ca/glaces-ice/>). The main source of data for the creation of these ice charts are the RADARSAT-2 ScanSAR images. Other sources of remote sensing data used are optical and thermal images (MODIS, VIIRS, Landsat, AVHRR, etc.) and passive microwaves (AMSR2). Auxiliary data, such as weather station and reanalysis data are also used to help determine the ice thickness stage. Knowing the data sources, expert sea ice analysts of the CIS manually identify regions of relatively homogenous ice conditions and identify the different ice types as well as their relative concentrations (in tenths) within these regions to produce the ice charts [30]. The ice charts show visually the dominant ice type and the ice concentrations of each ice polygon are estimated from visual interpretations of the ScanSAR imagery. It is important to clarify that during the winter season (after 1 January), the CIS merges MYI and SYI into one sea ice type called OI. This is due to the fact that during the winter in dry ice conditions, it is very difficult to differentiate between MYI and SYI using RADARSAT-2 ScanSAR imagery (main information source for ice chart creation). This is a limitation of C-band SAR in the discrimination between MYI and SYI in dry ice winter conditions.

The available sea ice charts indicate that Victoria Strait exhibited fast ice conditions from 1 December 2014 to 13 July 2015. This confirms that the ice was consolidated and immobile with no open water regions at the time of the image acquisitions in April 2015 and only the ice thickness changed. Given the fact that the study area exhibited fast ice conditions during the month of April

2015 with the air temperature being below zero during the entire month (Figure 2), the time difference between the acquisitions of the SAR images should not have effect in our study. According to the available ice charts, e.g., on 27 April 2015 (Figure 3a), the study area consisted of two main ice regimes: the first one dominated by OI (brown polygon intersects with the test site square in Figure 3a), and the second one dominated by thick FYI (dark green polygon intersects with the test site square in Figure 3a). Within the OI region the ice chart indicates that it contains 90% OI and 10% thick FYI and within the FYI region the ice chart indicates 100% FYI (see egg-codes in Figure 3a). Since, as mentioned above, the CIS merges MYI and SYI during the winter season (after 1 January) into one sea ice type called OI, we looked at the last 2014 regional ice chart (Figure 3b), which was created 29 December, and found that the OI region in the 27 April ice chart (Figure 3a) was classified as MYI (red polygon intersects with the test site square in Figure 3b). However, this MYI region in the 29 December ice chart (became OI region in the 27 April ice chart) was made up of 50% MYI, 40% SYI and 10% FYI (see egg-code in Figure 3b). Therefore, the 90% of OI reported in the 27 April ice chart is actually a mixture of MYI (50%) and SYI (40%).

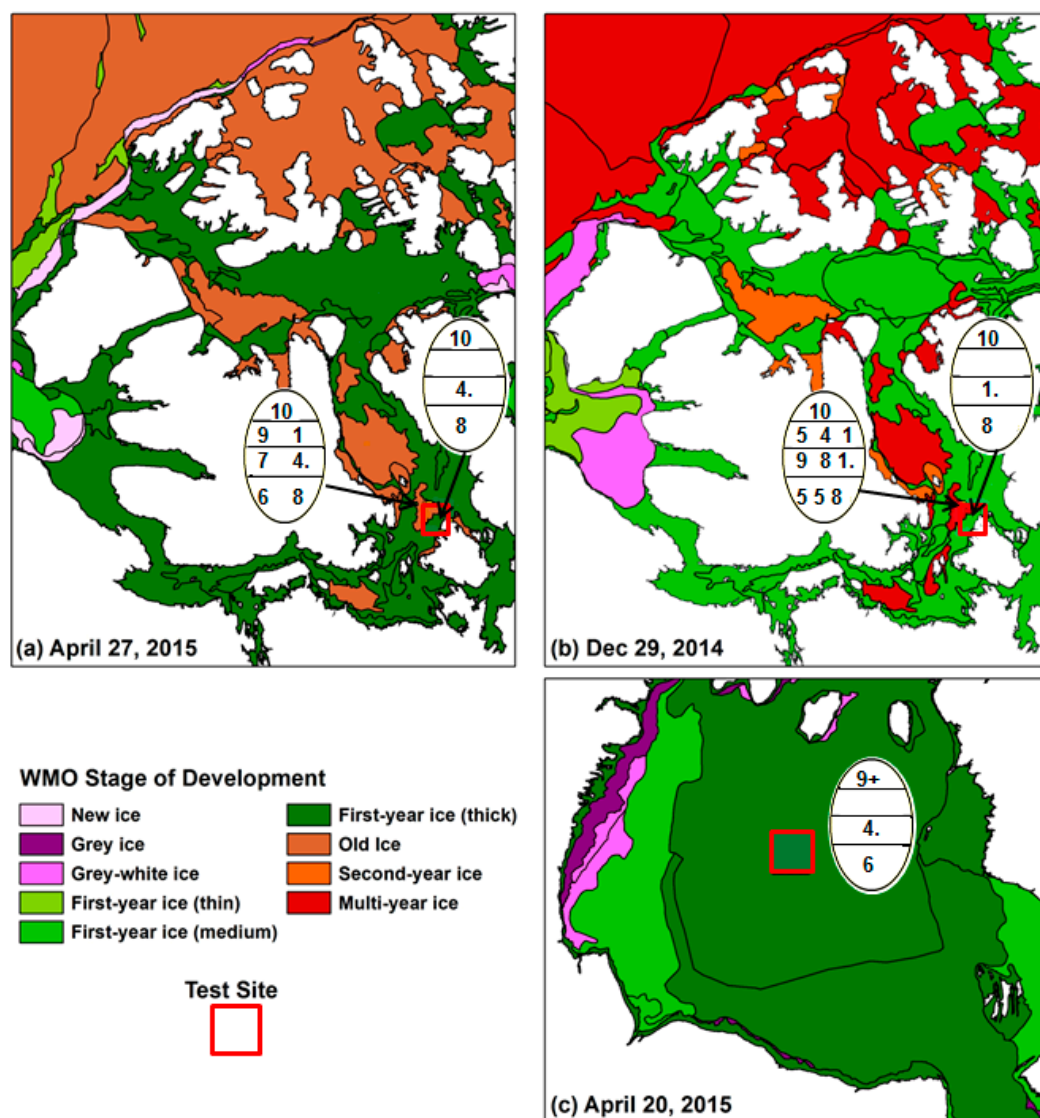


Figure 3. Ice charts of the CAA with egg-codes on (a) 27 April 2015 and (b) 29 December 2014. (c) Ice chart of Hudson Bay on 20 April 2015. Charts are according to the World Meteorology Organization (WMO) colors for sea ice stage of development.

Figure 3c shows the ice chart of 20 April 2015 over Hudson Bay which is the chart closest to the ALOS-2 image acquisition date (22 April 2015) used to test the classification results. This chart confirms that the area consisted of 100% FYI. Ice thickness data was also collected over the study area (Figure 1) to validate the ice types. This dataset was obtained during an airborne electromagnetic ice thickness survey on 19 April 2015 in the CAA [31]. It should be noted that the bottom of the study area contains a land portion in the ALOS-2 polarimetric SAR data, which was excluded from the processing using available coastline data.

3. Image Processing

Prior to the calculation of polarimetric parameters, a 7×7 refined Lee filter [32] was applied on all the available SAR data for noise despeckle. Next, 12 polarimetric parameters were calculated from the available full polarimetric SAR data over the study area, leading to three sets of parameters. One set was extracted from the RADARSAT-2 image and two sets were extracted from the two ALOS-2 images over the Victoria Strait. Table 2 presents the considered 12 polarimetric parameters along with their description. Sea ice types were manually sampled in the SAR imagery, using the ice chart of the study area (Figure 3a), by selecting representative polygons of FYI and OI over homogeneous areas. Most of the selected polygons were located in the overlap area between the RADARSAT-2 and the two ALOS-2 images. Figure 1 shows the selected samples as green and brown polygons for FYI and OI, respectively.

Table 2. Polarimetric parameters used in this study.

Short Form	Description
$\sigma_{HH}^0, \sigma_{VV}^0, \sigma_{HV}^0$	Sigma naught backscattering coefficients—linear horizontal or vertical transmit and horizontal or vertical receive polarization
SPAN	Total backscattering power, which is equal to the sum of the diagonal elements of the polarimetric coherency matrix ($T_{11} + T_{22} + T_{33}$)
$\sigma_{VV}^0/\sigma_{HH}^0, \sigma_{HV}^0/\sigma_{HH}^0, \sigma_{VH}^0/\sigma_{VV}^0$	Co- and cross-polarized ratios
ρ_{HHVV}	HH VV correlation coefficient [32]
H	Entropy [32]
A	Anisotropy [32]
α	Mean alpha angle [32]
δ_{HHVV}	HH VV phase difference [32]

Histograms of FYI and OI with their statistics were calculated for each parameter within each set and used to facilitate visual interpretation of the discrimination between the two ice classes. We used the Kolmogorov-Smirnov (K-S) distance [33] to estimate the separability between the two ice types in each polarimetric parameter. The K-S distance is a nonparametric separability criterion which measures the maximum absolute difference between two cumulative distribution functions, taking values between 0 and 1 [33]. We assume that a polarimetric parameter with discrimination capability between FYI and OI should provide a K-S distance > 0.5 . Furthermore, we group the polarimetric parameters with K-S distance > 0.5 into three categories:

- Category 1: includes parameters with some separability: $0.5 < \text{K-S distance} < 0.7$;
- Category 2: includes parameters with good separability: $0.7 \leq \text{K-S distance} < 0.9$;
- Category 3: includes parameters with very good separability: $0.9 \leq \text{K-S distance}$.

The 0.7 and 0.9 are reasonable threshold values to define the three aforementioned categories and were successfully used in different image processing and feature selection studies, e.g., [34,35]. Thus, using the calculated K-S distances, polarimetric parameters with discrimination capability

between FYI and OI are identified and groups based on the obtained K-S distance values are created. Since some of the identified polarimetric parameters might be correlated with each other, a correlation analysis was conducted on the polarimetric parameters with discrimination capability between FYI and OI. The correlation between parameters was estimated using the nonparametric Spearman correlation coefficient (R) [36]. The Spearman correlation varies between -1 and 1 and is insensitive to outliers [36]. Two parameters are considered strongly correlated if the absolute value of the correlation $R \geq 0.90$. The threshold value of 0.90 was selected since it was adopted and successfully used in [37,38]. Based on the obtained correlation values, the identified polarimetric parameters of each dataset can be divided into one or more groups of strongly correlated parameters and a group of independent (less correlated with $R < 0.90$) parameters. From each group of strongly correlated parameters, only one representative polarimetric parameter was selected and the rest are assumed redundant and excluded. For optimal selection, polarimetric parameter with the highest K-S distance between FYI and OI were selected. Finally, the selected polarimetric parameters together with the independent parameters (less correlated with $R < 0.90$) form a feature vector which can be used for sea ice classification. The classification was performed using the RF classification algorithm, which is an ensemble deep-learning classification technique [39]. The RF classification creates rule-based classification trees by generating multiple bootstrapped samples of the original training data and creating a series of nonparametric decision trees. Each tree is grown to the largest extent possible and the classification of each object is made by simple voting of all trees [39]. Half of the selected FYI and OI samples (Figure 1) were used to train the RF classifier and the other half to validate the results and estimate the classification accuracy.

4. Results Analysis

4.1. Histogram Interpretation

A total of 36 histograms of FYI and OI were calculated: 12 from the RADARSAT-2 and 24 from the two ALOS-2 SAR images over the Victoria Strait. As illustrated in Figure 4, the separability between FYI and OI is achievable for the case of C-band in four out of the twelve parameters; σ_{HH}^0 , σ_{VV}^0 , and σ_{HV}^0 backscattering coefficients and the SPAN. The highest absolute difference between the means of FYI and OI is given by the σ_{VV}^0 parameter (7.75 dB), while the minimum absolute difference is given by the σ_{HV}^0 parameter (6.31 dB). As shown in Figure 4, the mean values of the σ_{HH}^0 , σ_{VV}^0 , and σ_{HV}^0 backscattering coefficients are higher than the NESZ for RADARSAT-2. The remaining eight parameters provide poor discrimination between the two ice types.

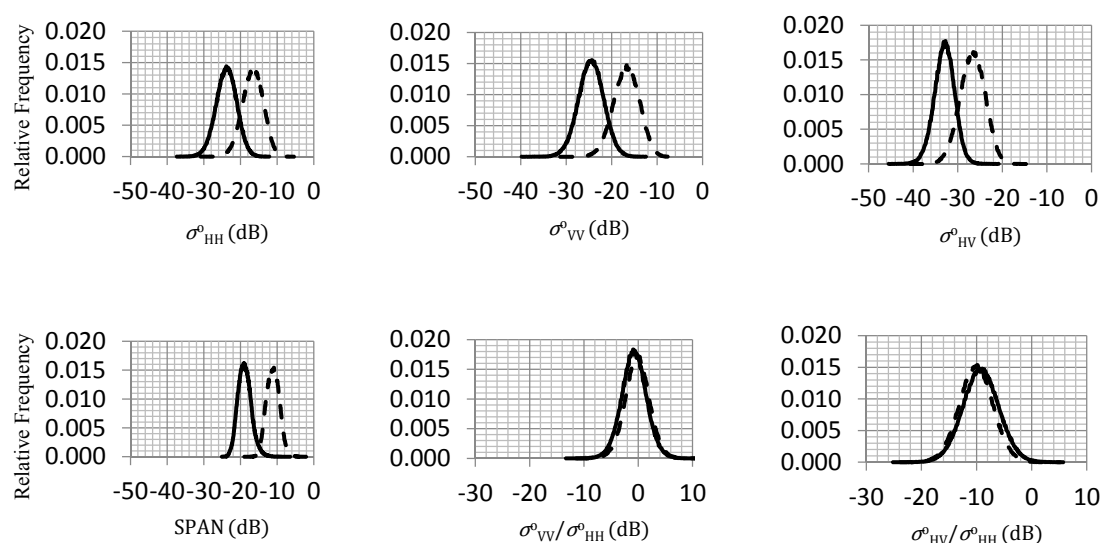


Figure 4. Cont.

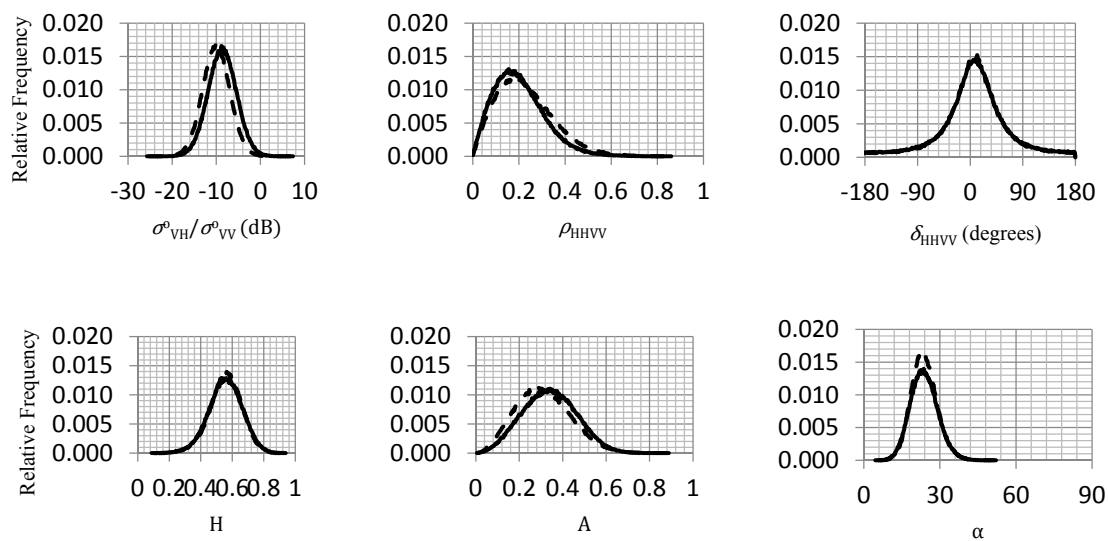


Figure 4. Histograms of polarimetric SAR parameters for the case of RADARSAT-2 data. Solid line refers to FYI and dashed line refers to OI.

Similar plots to those in Figure 4 were presented in [40] for smooth FYI (similar to the FYI in our case study) obtained using two RADARSAT-2 images acquired over a test site located in the CAA. We note that the mean values of the σ_{HH}^0 and σ_{VV}^0 backscattering coefficients and the SPAN in [40] are higher than the values shown in Figure 4. Also, the ρ_{HHV} and A parameters are higher in [40] compared to Figure 4. In contrary, the H and α parameters indicate lower values in [40] compared to the values shown in Figure 4. These observed differences should be related to the large difference in the radar incidence angles in the two case studies (40.9° in our case study and 27° and 23° in [40]). Also, the difference in the geophysical properties of the ice in the two case studies contributes in the observed differences, especially for the second RADARSAT-2 image in [40] since the air temperature was above zero few hours before the image acquisition.

Histograms of FYI and OI in each polarimetric parameter of the two ALOS-2 images are shown in Figure 5, with the mean values of the σ_{HH}^0 , σ_{VV}^0 , and σ_{HV}^0 backscattering coefficients being higher than the NESZ for ALOS-2. As illustrated in Figure 5, the discrimination between FYI and OI in L-band is poor in almost all the polarimetric parameters with the slight exception of the SPAN and H parameters. The absolute difference between the means of FYI and OI in the SPAN parameter is small at 2.02 dB and 2.17 dB for the 5 April and 28 April images, respectively. For the H parameter, the absolute difference between means is also small at 0.19 and 0.15 for 5 April and 28 April images, respectively. It should be noted in Figure 5 that the H parameter for L-band SAR data covers a wide range of values, indicating the presence of one main scattering mechanism and secondary scattering mechanisms [20].

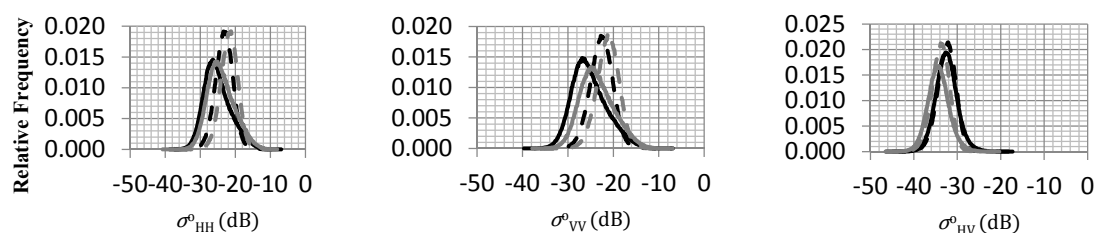


Figure 5. Cont.

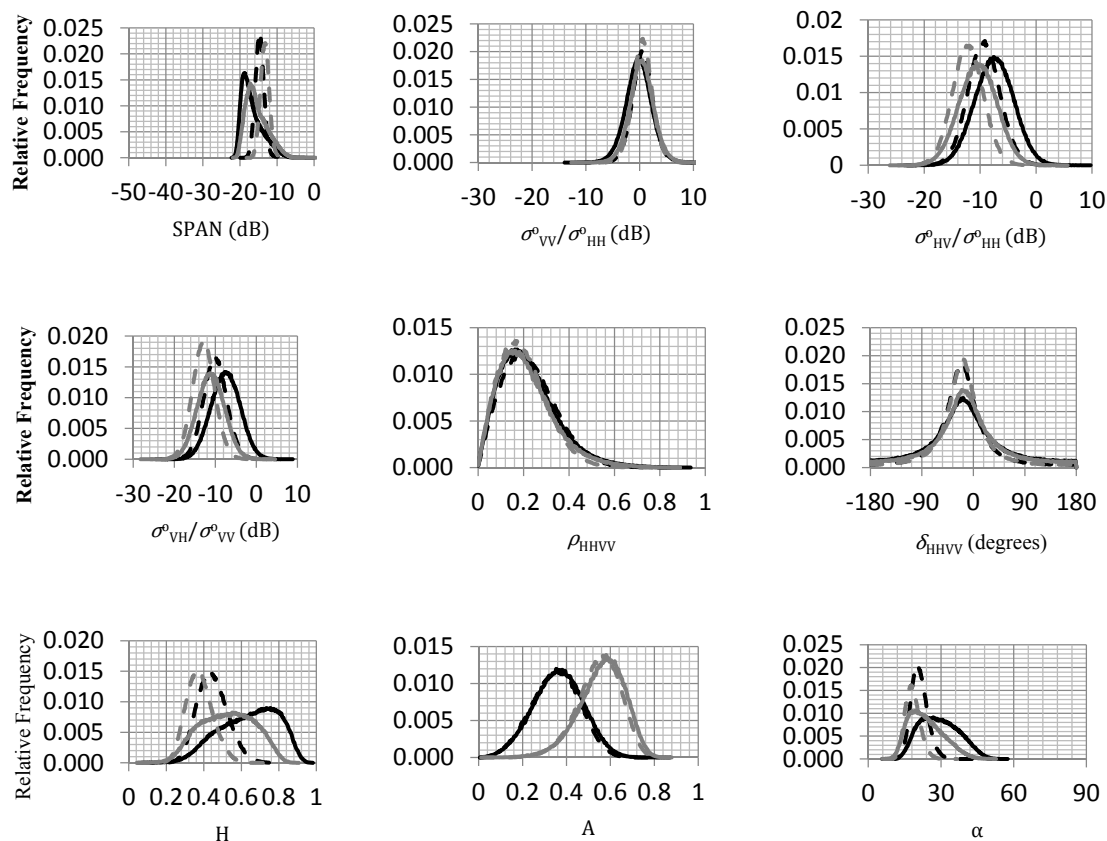


Figure 5. Histograms of polarimetric SAR parameters for the case of ALOS-2 data. Solid line refers to FYI and dashed line refers to OI. Black lines refer to the image acquired on 5 April 2015, while gray lines refer to the image acquired on 28 April 2015.

In [22], similar plots to those in Figure 5 were presented over four test sites, but for the σ_{HH}^0 backscattering coefficient only. Thus, a comparison of the plots in the two studies would show that the histograms of FYI and OI for the σ_{HH}^0 backscattering coefficient shown in Figure 5 agree with those presented for the test sites 3 and 4 in [22]. Different plots with increased discrimination capability between FYI and OI were shown in [22] for the test sites 1 and 2. This should be related to the fact that the test sites 1 and 2 were located in the radar far range with large radar incidence angles $>38^\circ$, while the test sites 3 and 4 were located in the radar near range with radar incidence angles close to those in our case study.

As we see in Figures 4 and 5, most of the histograms of FYI and OI in the investigated polarimetric parameters do not conform to normal distributions. This suggests that the use of parametric criteria which assume the normal distribution of the sea ice types within these parameters could be inaccurate. Thus, as seen in the subsequent sections, the analysis of FYI and OI in the different polarimetric parameters is performed using nonparametric criteria to avoid assumptions about the statistical distributions of the two ice types.

4.2. Separability Estimation

The discrimination between FYI and OI in the derived polarimetric parameters was quantitatively evaluated using the K-S distance [33] and the results are summarized in Table 3. As shown in Table 3, four out of the twelve polarimetric parameters can discriminate between FYI and OI (K-S distance > 0.5) in C-band. These parameters are the σ_{HH}^0 , σ_{VV}^0 , and σ_{HV}^0 backscattering coefficients and the SPAN. The only parameter that falls in the third category of very good separability is the SPAN with K-S distance = 0.97. The σ_{HH}^0 , σ_{VV}^0 , and σ_{HV}^0 backscattering coefficients belong to the second category of

good separability. Overall, these results confirm the previously performed visual interpretation of the sea ice histograms (Figure 4).

Table 3. K-S distance between FYI and OI. Green cells refer to parameters with very good separability, yellow cells refer to parameters with good separability, and cyan cells refer to parameters with some separability.

Polarimetric Parameters	RADARSAT-2 $\theta = 40.9^\circ$	ALOS-2 (5 April Image) $\theta = 36.6^\circ$	ALOS-2 (28 April Image) $\theta = 31.1^\circ$
σ_{HH}^0	0.80	0.33	0.36
σ_{HV}^0	0.79	0.04	0.11
σ_{VV}^0	0.83	0.40	0.37
SPAN	0.97	0.55	0.55
$\sigma_{VV}^0 / \sigma_{HH}^0$	0.11	0.15	0.06
$\sigma_{HV}^0 / \sigma_{HH}^0$	0.11	0.24	0.25
$\sigma_{VH}^0 / \sigma_{VV}^0$	0.18	0.33	0.24
ρ_{HHVV}	0.09	0.03	0.05
H	0.02	0.60	0.53
A	0.11	0.04	0.07
α	0.02	0.54	0.43
δ_{HHVV}	0.01	0.11	0.09

For L-band SAR data (ALOS-2), Table 3 shows that the SPAN, H and α can provide discrimination capability between FYI and OI, but α is applicable only to the 5 April image. We note that only the SPAN is a consistent discrimination parameter between the two sea ice types for both C- and L-band. The exclusion of the α parameter due to the decrease in the K-S distance below 0.5 in the 28 April ALOS-2 image might be related to the smaller radar incidence angle of the 28 April image (31.1°) in comparison to 5 April image (36.6°). The radar incidence angle could also be responsible for the decrease in the K-S distance in the H parameter (from 0.6 to 0.53). As seen in Table 3, all the detected L-band polarimetric parameters with discrimination capability between FYI and OI belong to the category of some separability. Overall, the results for the SPAN and H parameters confirm the previously performed visual interpretation of the sea ice histograms (Figure 5).

4.3. Correlation Analysis

Based on the calculated Spearman correlation values, the polarimetric parameters are placed into groups of strongly correlated ($R \geq 0.9$) and independent (less correlated with $R < 0.9$) parameters (Table 4).

Table 4. Grouping of strongly correlated and independent polarimetric parameters.

RADARSAT-2		ALOS-2 (5 April Image)		ALOS-2 (28 April Image)
Strongly correlated Parameters	Independent Parameters	Strongly correlated Parameters	Independent Parameters	Independent Parameters
SPAN σ_{VV}^0	$\sigma_{HH}^0 \sigma_{HV}^0$	H α	SPAN	SPAN H

As shown in Table 4, for the RADARSAT-2 data, the SPAN and σ_{VV}^0 backscattering coefficient are strongly correlated ($R = 0.9$). Thus, one of the two polarimetric parameters can be selected to form a feature vector with the σ_{HH}^0 and σ_{HV}^0 backscattering coefficients (independent parameters). Herein, the SPAN is selected since it provides higher K-S distance (0.97) between FYI and OI (Table 3). For the ALOS-2 data, only the 5 April image contained strongly correlated parameters (Table 4), which are the H and α polarimetric parameters with $R = 0.92$. The H polarimetric parameter provides higher K-S distance (0.6) between FYI and OI and is selected to form a feature vector with the SPAN (independent parameter). Consequently, 5 April and 28 April images have identical feature vectors (Table 4).

It is important to mention that for the RADARSAT-2 data the Spearman correlation R between the SPAN and the σ_{HH}^0 backscattering coefficient was found to be equal to 0.89. This correlation value is just below the selected threshold value (0.90) which was set to define whether two polarimetric parameters are strongly correlated. Thus, the feature vector for the case of C-band SAR data could be reduced to include only the SPAN and the σ_{HV}^0 backscattering coefficient. Also, it should be noted that the feature vector for L-band data combines two types of information; the total backscattering power of the signal and the randomness of the backscattering process.

4.4. Classification and Validation

The extracted feature vectors of the three sets of polarimetric parameters are used for the classification of FYI and OI using the RF classification algorithm. Half of the collected FYI and OI samples were used to train the classification algorithm and the other half to validate the results. Figure 6a–c show the classification results with FYI in green and OI in brown overlaid on the 27 April ice chart with the predominant ice type color code. The validation of the classification results was performed using both the selected validation samples and the 27 April ice chart. The validation samples were used to estimate the accuracies of the classification results, shown in Table 5. As expected, high classification accuracy of FYI and OI is obtained by the C-band data, in comparison to the L-band (Table 5). This is because the C-band polarimetric parameters of the feature vector used in the RF classification showed higher discrimination capability between FYI and OI, compared to L-band (Table 3). An overall classification accuracy of 98.99% is achieved with Kappa coefficient equal to 0.977 for the RADARSAT-2 image. The overall accuracy drops down to 82.17% (Kappa = 0.636) and 81.85% (Kappa = 0.595) for the two L-band ALOS-2 images, respectively (Table 5).

Table 5. Validation of the FYI and OI classification results for different SAR bands.

	RADARSAT-2 (%)		ALOS-2 (5 April Image) (%)		ALOS-2 (28 April Image) (%)	
	OI	FYI	OI	FYI	OI	FYI
OI	99.30	1.64	93.29	23.41	90.80	33.47
FYI	0.70	98.36	6.71	76.59	9.20	66.53
Overall accuracy	98.99		82.17		81.85	
Kappa coefficient	0.977		0.636		0.595	

For further validation of the results using the 27 April ice chart, we compared the classification results with the available chart (Figure 6a–c). It is shown in Figure 6a–c that where the ice chart indicates the predominance of FYI (green), the classifications on all three images show a higher detected concentration of FYI with very little OI. Furthermore, it is shown in Figure 6a that where the ice chart indicates a predominance of OI (brown), the classification of the RADARSAT-2 image shows a higher detected concentration of OI. Less OI was detected by the ALOS-2 classifications (Figure 6b,c).

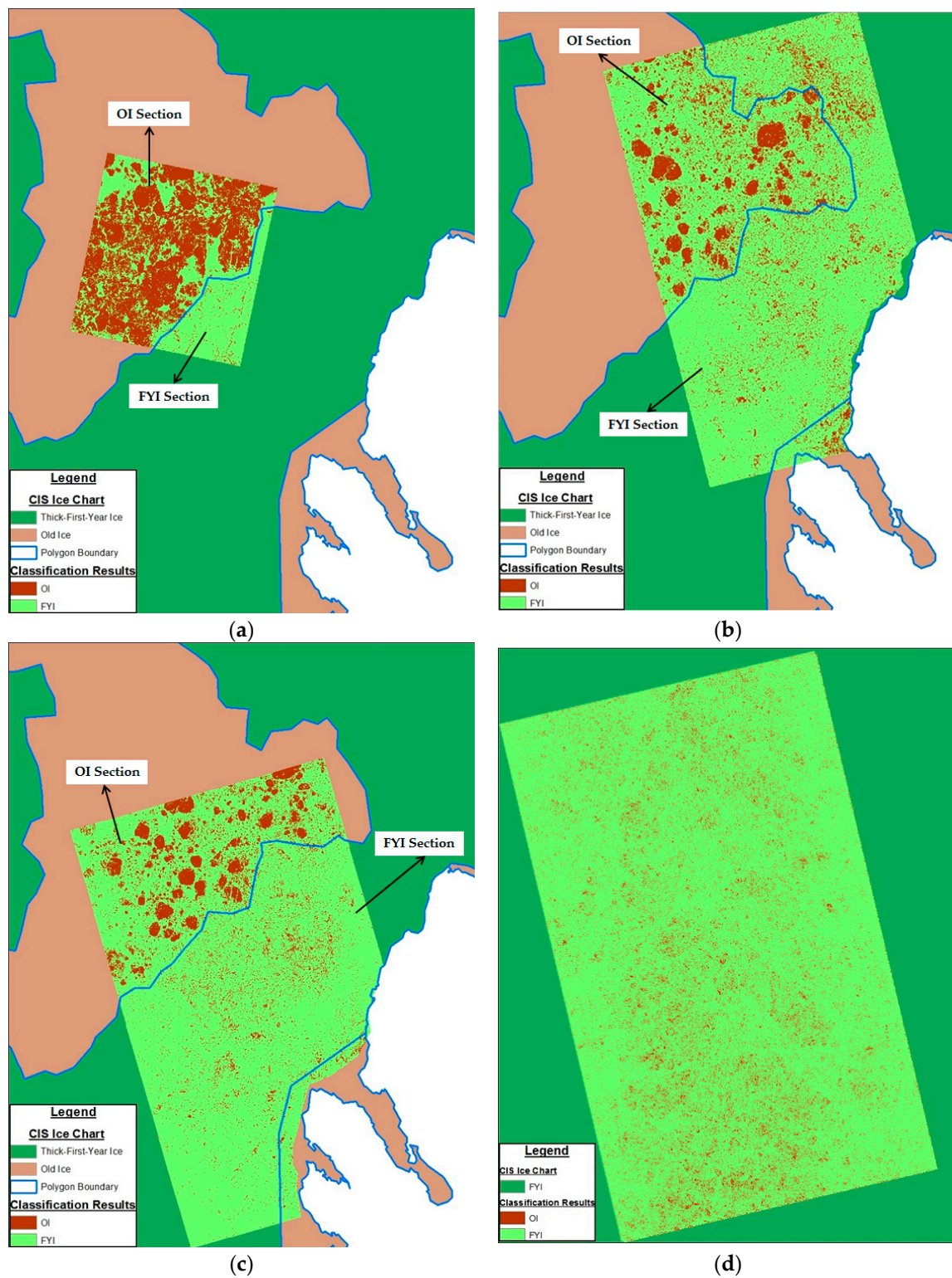


Figure 6. Overlay of the classification results of (a) RADARSAT-2 image, (b) 5 April ALOS-2 image and (c) 28 April ALOS-2 image over the sea ice chart valid for 27 April 2015. (d) Overlay of the classification results of Hudson Bay ALOS-2 image over the sea ice chart valid for 20 April 2015. Charts are according to the predominant ice type WMO color code.

Furthermore, the classifications in Figure 6a–c were separated into two sections (FYI and OI sections) corresponding to the FYI and OI polygons in the ice chart. Table 6 gives the concentrations, in tenths, of FYI and OI in the two sections and in the ice chart. The concentrations in each section were calculated with the ratio of pixels classified as FYI or OI over the total number of pixels within the section. In the FYI section (Figure 6a), the RADARSAT-2 classification results show similar results to the CIS ice chart (Table 6). As seen in Figure 6a, some linear features are detected as OI which are likely misclassified ridges between floes of FYI creating a strong backscatter signal. This result indicates that in areas of FYI predominance, the RADARSAT-2 classification have an error of less than 10%. The ALOS-2 images on the other hand (Figure 6b,c) show a lot more OI in the FYI section compared to the sea ice chart. With its higher penetration depth, the L-band signal detects more internal structures within the more malleable FYI [10]. In order to assess the potential error of OI detection in FYI areas, the previously trained RF classifiers which were used to classify the 5 April and 28 April ALOS-2 images were reapplied on the SPAN and H parameters of the ALOS-2 image over Hudson Bay (Figure 1) and results are shown in Figure 6d. As was shown in Figure 3c, the sea ice chart of this image valid on 20 April 2015 shows a predominance of thick FYI (green color), where no OI has ever been observed in this area. The classification accuracy of the Hudson Bay image calculated using selected validation samples (Figure 1) shows 2/10 of OI. This indicates a 20% error on the detection of FYI by the ALOS-2 classification. The results of Table 6 for the 5 April and 28 April ALOS-2 images are within that 20% margin of error when comparing to the RADARSAT-2 classification for the FYI section. This indicates a limitation of the L-band SAR that can misclassify regions of FYI as OI.

Table 6. Sea ice concentrations in the FYI and OI sections and ice chart shown in Figure 6a–c.

	FYI Section		OI Section	
	OI (in Tenths)	FYI (in Tenths)	OI (in Tenths)	FYI (in Tenths)
Sea Ice Chart	<1	9–10	9	1
RADARSAT-2 (Figure 6a)	1	9	7	3
ALOS-2 (Figure 6b)	3	7	4	6
ALOS-2 (Figure 6c)	3	7	4	6

The classification of all three images within the OI section shows less OI than the ice chart. The RADARSAT-2 classification shows more OI than the two ALOS-2 classifications (Table 6). As mentioned previously, after 1 January of each year, the CIS ice charts do not differentiate MYI from SYI and group them into one ice type called OI. This is because it is very difficult to distinguish both ice types in RADARSAT-2 ScanSAR imagery (main source of data for charts creation). Looking at the ice chart of 29 December 2014 (last ice chart in 2014 shown in Figure 3b), it indicates that the OI region in our study area consisted of 5/10 of MYI, 4/10 of SYI and 1/10 of FYI. The fact that our RADARSAT-2 classification detects less than 9/10 of OI could indicate that some of the SYI present in the OI section is not classified as OI. Figure 6b,c show 4/10 of well-defined floes of ice detected as OI. The detected 4/10 of OI is very close to the 5/10 of MYI in the 29 December 2014 ice chart. Given the shape and the percentage of the detected ice floes within the OI section, these results suggest that, with its higher penetration depth, L-band SAR can help discriminate MYI from SYI within the OI detected by C-band SAR. This finding was further validated by expert analysis from CIS, where it was confirmed that the rounded ice floes visible in the ALOS-2 classifications are related to MYI floes. The classification of the MYI floes by the L-band as OI means that the ice classified as FYI within the OI section includes also the SYI. We further validate the findings of our study using the available ice thickness data over close-up samples of the 28 April ALOS-2 SPAN image, the RADARSAT-2 SPAN image, and the 28 April ALOS-2 classification, selected within the OI section (Figure 7). As we can see in Figure 7, the ALOS-2 sample images show well-defined rounded shape MYI ice floes of different sizes. Between these ice floes, we can easily recognize deformed ice regions. These regions should be SYI (might also include FYI) which were formed due to pressure from the MYI floes in the

vicinity. These regions appear as bright regions because of the strong returned radar signal (due to the random backscattering). Also, small dark regions of smooth thick FYI are also visible in Figure 7. In the corresponding RADARSAT-2 image samples, the discrimination between the deformed SYI ice and the MYI floes is quite difficult. However, the smooth thick FYI regions can be easily seen (dark regions). Looking at the ice thickness data, we can see that the blue points (thickness $H \leq 2.0$ m) are associated with the small thick FYI regions, while the well-defined rounded shape MYI floes get yellow thickness points, with thickness values between 2 m and 3 m. Few red points of thickness >3 m are also existed over these floes. The thickness range of 2 m to 3 m is not uncommon in this area of the CAA for MYI floes, given that the ice floes drifted from the north to warmer waters in the far south [31]. Also, these specific ice floes have survived two melt seasons, as reported in [31]. As shown in Figure 7, the deformed SYI regions between the MYI floes (bright regions in ALOS-2 samples) get a mixture of yellow and red ice thickness points, indicating a wide variety of thickness values. In Figure 7, we also show the ice thickness data over the obtained classification results of the two 28 April ALOS-2 image samples. Herein, we see the detected MYI floes with thickness values between 2 m to 3 m (yellow points). Also, these classification samples show that the green ice class corresponds to the SYI and FYI, which is confirmed from the existence of blue ice thickness points (smooth thick FYI) and yellow and red ice thickness points (deformed SYI) over the green class. All the aforementioned analysis of the thickness data was also confirmed by a CIS expert sea ice analyst.

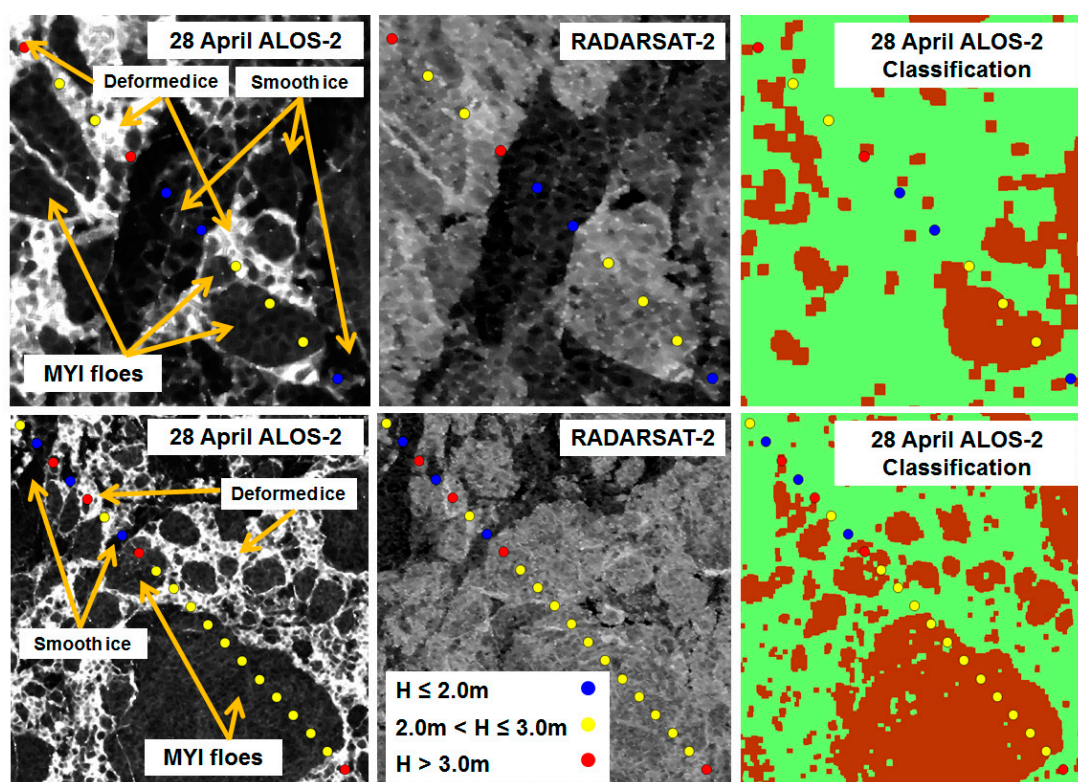


Figure 7. Ice thickness data overlaid on close-up samples of the 28 April ALOS-2 SPAN image, the RADARSAT-2 SPAN image, and the 28 April ALOS-2 image classification results.

From the aforementioned results, we note that the large difference in radar incidence angle between the 28 April ALOS-2 image and the RADARSAT-2 image ($\sim 10^\circ$) had no major effect on the results. This is because the results we obtained with the 5 April ALOS-2 image are similar to those which we obtained using the 28 April ALOS-2 image (only minor differences in e.g., classification accuracies in Table 5) and the difference in radar incidence angle between the 5 April ALOS-2 image and the RADARSAT-2 image is fairly small ($\sim 4^\circ$).

5. Conclusions

The potential of L-band SAR for sea ice type classification in dry ice winter conditions was investigated in this study. A set of polarimetric parameters were derived and evaluated to discriminate between FYI and OI, where the latter was a mixture of MYI and SYI. The discrimination capability of L-band SAR in each polarimetric parameter was compared with C-band SAR using collocated C-band SAR data. Between C- and L-band SAR, only the SPAN parameter was found consistent in the discrimination between FYI and OI. However, the SPAN showed some separability between FYI and OI for L-band SAR, though it was of very good separability for C-band data. In addition to the SPAN, the H parameter showed also some separability between FYI and OI but failed to provide any discrimination capability between the two sea ice types in the case of C-band. The α parameter was able to provide some separability between FYI and OI in the 5 April ALOS-2 image. However, the steeper incidence angle for the 28 April ALOS-2 image has likely reduced the discrimination capability leading to a K-S distance below the threshold value of 0.5. Information redundancy analysis through the estimation of correlation between identified polarimetric parameters with discrimination capability between FYI and OI was conducted for both C- and L-band SAR. The information redundancy analysis led to the extraction of feature vectors. The extracted feature vectors of the two ALOS-2 images were identical, containing the SPAN and the H parameters. The SPAN parameter was also one of the parameters of the extracted feature vector for C-band, in addition to the σ_{HH}^0 and σ_{HV}^0 backscattering coefficients. The extracted feature vectors were then used for the classification of sea ice and the accuracy of L-band SAR was found lower than that of C-band. However, results indicated that for L-band, well defined ice floes with rounded shape associated with the MYI within the OI region were detected. Identifying MYI from SYI has traditionally been extremely difficult from C-band SAR late in the consolidation season. Therefore, this could indicate a new potential application of L-band SAR to detect MYI floes within a mixture of MYI and SYI in dry ice winter conditions. It is important to mention that in the case of L-band, our study suggests that SYI was misclassified as FYI. Thus, improved ice classification results are likely possible with combined C- and L-band SAR imagery. The results of this study will be further validated using additional collocated C- and L-band SAR data at various radar incidence angles and under different weather and ice conditions. This will be the subject of our future work, though the acquisition of coincident RADARSAT-2 and ALOS-2 data over the Canadian Arctic is a challenge.

Acknowledgments: PALSAR-2 images were provided by Japan Aerospace Exploration Agency (JAXA) under the 4th Research Announcement program (PI NO. 1202, S. Howell). Authors would like to thank the anonymous reviewers for their constructive comments which have greatly improved the manuscript.

Author Contributions: Mohammed Dabboor conceived the study and processed the data. Mohammed Dabboor, Benoit Montpetit, and Stephen Howell analyzed the results. Christian Haas provided the ice thickness data. All authors contributed to the writing of the paper.

Conflicts of Interest: The authors declare no conflict of interest.

References

1. Shokr, M.; Sinha, N.K. *Sea Ice: Physics and Remote Sensing*; John Wiley & Sons: Hoboken, NJ, USA, 2015; ISBN 978-1-119-02789-8.
2. Drinkwater, M.R.; Early, D.S.; Long, D.G. ERS-1 Investigations of Southern Ocean Sea Ice Geophysics Using Combined Scatterometer and SAR Images. In Proceedings of the IEEE Geoscience and Remote Sensing Symposium, Pasadena, CA, USA, 8–12 August 1994; pp. 165–167.
3. Johannessen, J.A. Overview of ERS-1 Scientific Results Obtained from Ocean and Sea Ice Observations. In Proceedings of the IEEE Geoscience and Remote Sensing Symposium, Firenze, Italy, 10–14 July 1995; pp. 1035–1037.
4. Morris, K.; Jeffries, M.O.; Li, S. Sea Ice Characteristics and Seasonal Variability of ERS-1 SAR Backscatter in the Bellingshausen Sea. In *Antarctic Sea Ice: Physical Processes, Interactions and Variability*; American Geophysical Union: Washington, DC, USA, 1998.

5. Leppäranta, M.; Sun, Y.; Haapala, J. Comparisons of sea-ice velocity fields from ERS-1 SAR and a dynamic model. *J. Glaciol.* **1998**, *44*, 248–262. [\[CrossRef\]](#)
6. Kaleschke, L.; Lüpkes, C.; Vihma, T.; Haarpaitner, J.; Bochert, A.; Hartmann, J.; Heygster, G. Validation of a high resolved SSM/I sea ice algorithm using airborne and ERS-2 SAR data and atmospheric models. *Can. J. Remote Sens.* **2001**, *27*, 526–536. [\[CrossRef\]](#)
7. Kaleschke, L.; Kern, S. ERS-2 SAR Image Analysis for Sea Ice Classification in the Marginal Ice Zone. In Proceedings of the IEEE International Geoscience and Remote Sensing Symposium, Toronto, ON, Canada, 24–28 June 2002; pp. 3038–3040.
8. Johannessen, O.M.; Alexandrov, V.Y.; Frolov, I.Y.; Bobylev, L.P.; Sandven, S.; Pettersson, L.H.; Kloster, K.; Babich, N.G.; Mironov, Y.U.; Smirnov, V.G. *Remote Sensing of Sea Ice in the Northern Sea Route: Studies and Applications*; Springer-Praxis: Berlin, Germany, 2007; ISBN 978-3-540-48840-8.
9. Karvonen, J.; Simila, M.; Makynen, M. Open water detection from Baltic Sea ice Radarsat-1 SAR imagery. *IEEE Geosci. Remote Sens. Lett.* **2005**, *2*, 275–279. [\[CrossRef\]](#)
10. Arkett, M.; Flett, D.; De Abreu, R.; Clemente-Colon, P.; Woods, J.; Melchior, B. Evaluating ALOS-PALSAR for Ice Monitoring—What Can L-Band Do for The North American Ice Service? In Proceedings of the IEEE Geoscience and Remote Sensing Symposium, Boston, MA, USA, 7–11 July 2008; pp. V-188–V-191.
11. Barber, D.G.; Yackel, J.J.; Hanesiak, J.M. Sea ice, RADARSAT-1 and arctic climate processes: A review and update. *Can. J. Remote Sens.* **2014**, *27*, 51–61. [\[CrossRef\]](#)
12. Drinkwater, M.R.; Kwok, R.; Winebrenner, D.P.; Rignot, E. Multifrequency polarimetric synthetic aperture radar observations of sea ice. *J. Geophys. Res.* **1991**, *96*, 20679–20698. [\[CrossRef\]](#)
13. Shokr, M.; Dabboor, M. Interannual variability of young ice in the arctic estimated between 2002 and 2009. *IEEE Trans. Geosci. Remote Sens.* **2013**, *51*, 3354–3370. [\[CrossRef\]](#)
14. Johansson, A.M.; King, J.A.; Doulgeris, A.P.; Gerland, S.; Singha, S.; Spreen, G.; Busche, T. Combined observations of Arctic sea ice with near-coincident collocated X-band, C-band, and L-band SAR satellite remote sensing and helicopter-borne measurements. *J. Geophys. Res. Oceans* **2017**, *122*, 669–691. [\[CrossRef\]](#)
15. Lehtiranta, J. Comparison of C- and L-Band Synthetic Aperture Radar Images for Sea Ice Motion Estimation. Master's Thesis, Aalto University, Helsinki, Finland, 2013.
16. Dierking, W.; Busche, T. Sea ice monitoring by L-band SAR: An assessment based on literature and comparisons of JERS-1 and ERS-1 imagery. *IEEE Trans. Geosci. Remote Sens.* **2006**, *44*, 957–970. [\[CrossRef\]](#)
17. Eriksson, L.E.B.; Borenäs, K.; Dierking, W.; Berg, A.; Santoro, M.; Pemberton, P.; Lindh, H.; Karlson, B. Evaluation of new spaceborne SAR sensors for sea-ice monitoring in the Baltic Sea. *Can. J. Remote Sens.* **2010**, *36*, S56–S73. [\[CrossRef\]](#)
18. Lehtiranta, J.; Siiri, S.; Karvonen, J. Comparing C- and L-band SAR images for sea ice motion estimation. *Cryosphere* **2015**, *9*, 357–366. [\[CrossRef\]](#)
19. Dierking, W. Mapping of different sea ice regimes using images from Sentinel-1 and ALOS synthetic aperture radar. *IEEE Trans. Geosci. Remote Sens.* **2010**, *48*, 1045–1058. [\[CrossRef\]](#)
20. Scheuchl, B.; Caves, R.; Cumming, I.; Staples, G. H/A/a-Based Classification of Sea Ice Using SAR Polarimetry. In Proceedings of the 23rd Canadian Symposium on Remote Sensing, Sainte-Foy, QC, Canada, 21–24 August 2001.
21. Berg, A. Spaceborne Synthetic Aperture Radar for Sea Ice Observations, Concentration and Dynamics. Ph.D. Thesis, Chalmers University of Technology, Göteborg, Sweden, 2014.
22. Casey, J.A.; Howell, S.E.; Tivy, A.; Haas, C. Separability of sea ice types from wide swath C- and L-band synthetic aperture radar imagery acquired during the melt season. *Remote Sens. Environ.* **2016**, *174*, 314–328. [\[CrossRef\]](#)
23. Nakamura, K.; Wakabayashi, H.; Naoki, K.; Nishio, F.; Moriyama, T.; Uratsuka, S. Observation of sea-ice thickness in the Sea of Okhotsk by using dual-frequency and fully polarimetric airborne SAR (Pi-SAR) data. *IEEE Trans. Geosci. Remote Sens.* **2005**, *43*, 2460–2469. [\[CrossRef\]](#)
24. Wakabayashi, H.; Matsuoka, T.; Nakamura, K.; Nishio, F. Polarimetric characteristics of sea ice in the sea of Okhotsk observed by airborne L-band SAR. *IEEE Trans. Geosci. Remote Sens.* **2004**, *42*, 2412–2425. [\[CrossRef\]](#)
25. Kaleschke, L.; Maaß, N.; Haas, C.; Hendricks, S.; Heygster, G.; Tonbøe, A. A sea-ice thickness retrieval model for 1.4 GHz radiometry and application to airborne measurements over low salinity sea-ice. *Cryosphere* **2010**, *4*, 583–592. [\[CrossRef\]](#)

26. Huntemann, M.; Heygster, G.; Kaleschke, L.; Krumpen, T.; Mäkynen, M.; Drusch, M. Empirical sea ice thickness retrieval during the freeze-up period from SMOS high incident angle observations. *Cryosphere* **2014**, *8*, 439–451. [[CrossRef](#)]
27. Kwok, R.; Cunningham, G.F. Seasonal ice area and volume production of the Arctic Ocean: November 1996 through April 1997. *J. Geophys. Res.* **2002**, *107*, 8038. [[CrossRef](#)]
28. Zhang, B.; Perrie, W.; Li, X.; Pichel, W.G. Mapping sea surface oil slicks using RADARSAT-2 quad-polarization SAR image. *Geophys. Res. Lett.* **2011**, *38*, L10602. [[CrossRef](#)]
29. Shimada, M.; Watanabe, M.; Motooka, T.; Kankaku, Y.; Suzuki, S. Calibration and validation of the PALSAR-2. In Proceedings of the 2013 Asia-Pacific Conference on Synthetic Aperture Radar (APSAR), Tsukuba, Japan, 23–27 September 2013.
30. Meteorological Service of Canada. *MANICE: Manual of Standard Procedures for Observing and Reporting Ice Conditions*, 9th ed.; Canadian Ice Service, Environment Canada: Ottawa, ON, Canada, 2005.
31. Haas, C.; Howell, S. Ice thickness in the Northwest Passage. *Geophys. Res. Lett.* **2015**, *42*, 7673–7680. [[CrossRef](#)]
32. Lee, J.S.; Pottier, E. *Polarimetric Radar Imaging: From Basic to Applications*; CRC Press, Taylor & Francis Group: Boca Raton, FL, USA, 2009.
33. Duda, R.; Hart, P.; Stork, D. *Pattern Classification*, 2nd ed.; John Wiley & Sons: New York, NY, USA, 2000; ISBN 978-0-471-05669-0.
34. Ko, K.T. A Hybrid Road Identification System Using Image Processing Techniques and Back-Propagation Neural Networks. Master's Thesis, Mississippi State University, Oktibbeha County, MS, USA, 1995.
35. Desbordes, P.; Ruan, S.; Modzelewski, R.; Pineau, P.; Vauclin, S.; Gouel, P.; Michel, P.; Di Fiore, F.; Vera, P.; Gardin, I. Predictive value of initial FDG-PET features for treatment response and survival in esophageal cancer patients treated with chemo-radiation therapy using a random forest classifier. *PLoS ONE* **2017**, *12*, e0173208. [[CrossRef](#)] [[PubMed](#)]
36. Press, W.; Teukolsky, S.A.; Vetterling, W.; Flannery, B. *Numerical Recipes, The Art of Scientific Computing*, 3rd ed.; Cambridge University Press: Cambridge, UK, 2007; ISBN 0521880688.
37. Geldsetzer, T.; Arkett, M.; Zagon, T.; Charbonneau, F.; Yackel, J.; Scharien, R. All-season compact-polarimetry C-band SAR observations of sea ice. *Can. J. Remote Sens.* **2015**, *41*, 485–504. [[CrossRef](#)]
38. Todorova, L.; Vassilev, P.; Surchev, J. Using Phi Coefficient to Interpret Results Obtained by InterCriteria Analysis. In *Advances in Intelligent Systems and Computing*; Springer: Cham, Switzerland, 2016; Volume 401, pp. 231–239.
39. Breiman, L. Random forests. *Mach. Learn.* **2001**, *45*, 5–32. [[CrossRef](#)]
40. Gill, J.; Yackel, J.J.; Geldsetzer, T. Analysis of consistency in first-year sea ice classification potential of C-band SAR polarimetric parameters. *Can. J. Remote Sens.* **2013**, *39*, 101–117. [[CrossRef](#)]

